Chemical Science

ROYAL SOCIETY OF CHEMISTRY

EDGE ARTICLE

View Article Online
View Journal | View Issue

Cite this: *Chem. Sci.*, 2025, **16**, 18201

All publication charges for this article have been paid for by the Royal Society of Chemistry

A cyanate-functionalized polymer composite electrolyte with a self-healing gradient SEI affords ultra-thermally stable lithium batteries

Jiakai Wang,[a] Siyu Zhang,[a] Linchen Zhang,[a] Shenzhen Deng,[a] Yuanyuan Sun,[a] Yimou Wang,[a] Jinglin Wang,[c] Weidong Zhou,*[b] Zhongtao Li*[a] and Mingbo Wu[a]

Solid-state electrolytes can significantly enhance the thermal stability of batteries and reduce the risk of thermal runaway. Polymer/ceramic composite electrolytes hold promise for addressing the solid/solid interface contact issues in solid-state batteries. However, high-temperature environments can exacerbate the interfacial phase separation of polymer/ceramics, hindering barrier lithium-ion transport and intensifying side reactions on the anode. To extend the working temperature up to 160 °C, a high-thermal-stability polymer electrolyte containing cyano and ester–urea groups was *in situ* polymerized with porous lithium iron phosphate ($Li_{1.3}Al_{0.3}Ti_{1.7}(PO_4)_3$). The cyano groups in PPEM suppress interfacial phase separation through strong coordination with Ti^{4+} sites on LATP, whereas the ester–urea segments promote Li^+ transport. This dual-functional design achieved a lithium-ion transference number of 0.78 at room temperature. Moreover, a self-healing gradient solid electrolyte interphase (SEI) layer formed spontaneously during cycling, featuring a highly ion-conductive inner Li_3N layer and an outer crosslinked polymer layer for mechanical reinforcement, which effectively suppresses lithium dendrite growth and side reactions at elevated temperatures. The synergistic effect of phase separation inhibition and SEI healing enables the Li/PPEM–LATP/Li symmetric cell to cycle stably for 2400 h at 0.2 mA cm^{-2} and the Li/PPEM–LATP/LFP pouch cell (0.5 Ah) to retain 91% capacity after 100 cycles at 160 °C/0.5C. Furthermore, the PPEM–LATP electrolyte exhibited a wide electrochemical window (>5.4 V) and exceptional thermal resilience, with no thermal runaway observed below 312.3 °C in abuse tests. This study establishes a paradigm for designing high-temperature-resistant solid-state electrolytes *via* interface-engineering strategies.

Received 9th July 2025
Accepted 27th August 2025

DOI: 10.1039/d5sc05102a

rsc.li/chemical-science

Introduction

In traditional lithium-ion batteries, the electrolyte tends to decompose at high temperatures, generating gases and heat, which leads to a rapid increase in the internal pressure and temperature within the battery, triggering thermal runaway.[1–7] Meanwhile, the solid electrolyte interphase (SEI) on the anode also undergoes side reactions at elevated temperatures, further exacerbating the risk of thermal runaway.[8] Thus, enhancing the temperature tolerance of batteries is crucial for addressing battery safety issues caused by thermal runaway at high temperatures. To address these issues, replacing traditional liquid electrolytes with thermally stable solid-state electrolytes has emerged as an effective solution.[9] Solid-state electrolytes, especially ceramic electrolytes, exhibit excellent thermal and chemical stability, maintaining a stable structure and high ionic conductivity under high-temperature conditions, thereby significantly enhancing battery thermal stability and reducing the risk of thermal runaway.[10–12]

However, rigid ceramic electrolytes suffer from solid/solid interface contact issues, leading to a continuous increase in interfacial impedance during cycling and eventual battery failure. Previous studies have used flexible polymers to repair the solid/solid interface.[13–15] The development of inorganic/polymer composite solid-state electrolytes (CSEs) has partially resolved the contact problems between inorganic materials and electrodes.[16,17] However, the interfacial compatibility between polymers and ceramic electrolytes remains poor, causing the aggregation of heterogeneous particles and reducing the efficiency of Li^+ transport. High-temperature conditions further exacerbate interfacial phase separation between inorganic and polymer components, intensifying this issue. Consequently, the reported composite solid-state electrolytes still suffer from low ionic conductivity and poor thermal stability.[18] Moreover, high

[a]*State Key Laboratory of Heavy Oil Processing, College of Chemical Engineering, China University of Petroleum (East China), Qingdao, 266580, P. R. China. E-mail: liztao@upc.edu.cn*

[b]*State Key Laboratory of Organic-Inorganic Composites, Beijing University of Chemical Technology, Beijing, 100029, China. E-mail: zhouwd@mail.buct.edu.cn*

[c]*Department of Hepatobiliary Surgery, Hepatobiliary Institute of Nanjing Drum Tower Hospital, Medical School of Nanjing University, Nanjing, 210008, P. R. China*

temperatures can accelerate side reactions and thermal feedback at the polymer composite solid-state electrolyte/Li interface, which is detrimental to the formation of a stable SEI layer on the anode. Therefore, developing inorganic/polymer composite solid-state electrolytes with good interfacial compatibility is an effective way to enhance the ionic conductivity and thermal stability of the electrolyte.[19]

Based on this, the development of high-temperature solid-state batteries can be achieved through the following approaches: (1) enhancing the interaction between inorganic and polymer electrolytes to improve interfacial compatibility at high temperatures and stabilize ionic transport across the internal interfaces of the composite solid-state electrolyte;[20–23] (2) forming a structurally stable and self-healing SEI layer on the Li anode interface to suppress high-temperature side reactions.[17,24] Herein, we synthesized a monomer containing polar groups, such as ester–urea bonds and cyano groups (MAUN), and copolymerized it *in situ* with porous $Li_{1.3}Al_{0.3}Ti_{1.7}(PO_4)_3$ (LATP) to develop a novel composite solid-state electrolyte (PPEM–LATP). The polymer in PPEM–LATP contains unsaturated bonds, such as cyano groups, which can coordinate with LATP to enhance the interfacial compatibility between inorganic oxides and polymer electrolytes, thereby forming an interface conducive to Li^+ transport. The PPEM–LATP composite electrolyte achieved an ionic conductivity of 7.2×10^{-4} S cm^{-1} at room temperature, with a Li^+ transference number of 0.78. Meanwhile, the polymer monomer adsorbs onto the lithium anode surface *via* weak C≡N–Li^+ interactions, forming a gradient-structured SEI layer. The inner layer of this SEI is rich in Li_3N, which facilitates efficient Li^+ transport, while the outer layer is a flexible organic interface that effectively suppresses lithium dendrite formation and high-temperature side reactions, thereby enhancing the cycling stability and safety of the battery.[25–27] Additionally, MAUN exhibits higher electrochemical and thermal stabilities (electrochemical window > 5.8 V, thermal decomposition temperature > 300 °C). The Li/PPEM–LATP/LFP all-solid-state battery assembled with this electrolyte can operate normally at 150 °C and maintain extremely high safety under thermal abuse conditions.

Results and discussion

Characteristics of cyanate polymer electrolytes

In a typical synthesis (Fig. 1a), to this biphasic system, 4 mL of 3-hydroxypropionitrile (HPN) precursor was introduced *via* syringe followed by sequential addition of 0.5 mL triethylamine (TEA) as a phase-transfer catalyst and 7 mL of isocyanatoethyl methacrylate (IEM) monomer under vigorous magnetic stirring. Upon completion, the reaction mixture underwent sequential liquid–liquid extraction. The organic phase was then subjected to rotary evaporation under reduced pressure. Final purification was achieved through lyophilization under high vacuum ($<10^{-3}$ mbar) for 18 hours, yielding the MAUN monomer as an off-white crystalline solid. A polymer precursor solution was prepared by dissolving poly(ethylene glycol) methyl ether acrylate (PEGMA, M_w = 480 g mol^{-1}) and MAUN monomer at a molar ratio of 6 : 1. This was followed by the incorporation of 20 wt% lithium bis(trifluoromethanesulfonyl)imide (LiTFSI) and azo biisobutyronitrile (AIBN). The mixture underwent rigorous magnetic stirring until achieving optically transparent viscosity (as shown in the optical photo, PPEM).

In the ^{1}H NMR spectra of PEGMA and MAUN (Fig. S1), the characteristic peaks of CH_2=CH at 5.62 and 6.13 ppm disappeared after polymerization, while a new peak for –CH_2–CH_2– appeared at 1.5 ppm.[28] Fourier-transform infrared spectroscopy (FTIR) was further employed to characterize the polymerization degree, as shown in Fig. S2. The disappearance of the infrared absorption peaks at 3030 and 1635 cm^{-1}, corresponding to the stretching vibrations of =C–H and C=C, confirmed the completion of polymerization, consistent with the ^{1}H NMR results. Differential scanning calorimetry (DSC) (Fig. S3) revealed that the introduction of MAUN lowered the glass transition temperature (T_g) from 85.85 to 84.89 °C.[29] The introduction of bulky groups, such as cyano and urea, increases the polymer chain spacing, alters the entanglement and packing of the polymer chains, and reduces the crystallization temperature. Thermogravimetric analysis (TGA) (Fig. 1b) indicated superior thermal stability for PPEM, with a decomposition onset at 300 °C (mass loss > 5%) *versus* 248 °C for PPE, underscoring its suitability for extreme (>100 °C) operational environments.

Fourier-transform infrared (FT-IR) spectroscopy (Fig. 1c) revealed a significant redshift of the S–N–S stretching vibration from 744.36 cm^{-1} (PPE matrix) to 739.83 cm^{-1} upon PPEM incorporation. The spectral shift provides compelling evidence for the formation of increased contact ion pairs (CIPs), which arise from the weakened electrostatic interaction between Li^+ and $TFSI^-$ anions induced by cyano-functionalized moieties. Density functional theory (DFT) calculations (Fig. 1d) demonstrated that LiTFSI dissociation energy decreased from 5.039 eV (in pure LiTFSI) to 4.395 eV in the presence of PPEM, confirming that cyanide groups enhance salt dissociation. Fig. 1e further elucidates the coordination state of $TFSI^-$, with the Raman spectra divided into two parts: free $TFSI^-$ (740 cm^{-1}) and bonded ion pairs (744 cm^{-1}). The proportion of free $TFSI^-$ (64.3%) in PPEM was much higher than that in PPE (42.5%) when the composition of different Li^+ species was quantitatively analyzed by peak area deconvolution, which was due to the cyano-rich groups in PPEM that promoted the dissociation of lithium salts. As shown in Fig. 1f, the broad A_1 peak in the upstream region indicates that the Li^+ species formed a strong coordination structure with the TFSI and C=O units. The sharp A_2 peak downstream corresponds to the disordered Li^+ environment. Notably, the fractional contribution of non-coordinating Li^+ species (A_2 environment) increased from 26% in PPE to 42% in PPEM. Hence, MAUN plays an important role in regulating the local environment of Li^+ by decoupling Li^+–TFSI and Li^+–O ion pairs, resulting in a significant downfield shift of the Li^+ resonant peak, corroborating the presence of loosely coordinated Li^+ species in the PPEM matrix. Electrochemical validation was conducted using Li//PPEM//Li symmetric cells (Fig. 1g). The PPEM-based electrolyte exhibited exceptional interfacial stability, maintaining stable cycling for over 2000 h at a current density of 0.2 mA cm^{-2}. Subsequently, as the

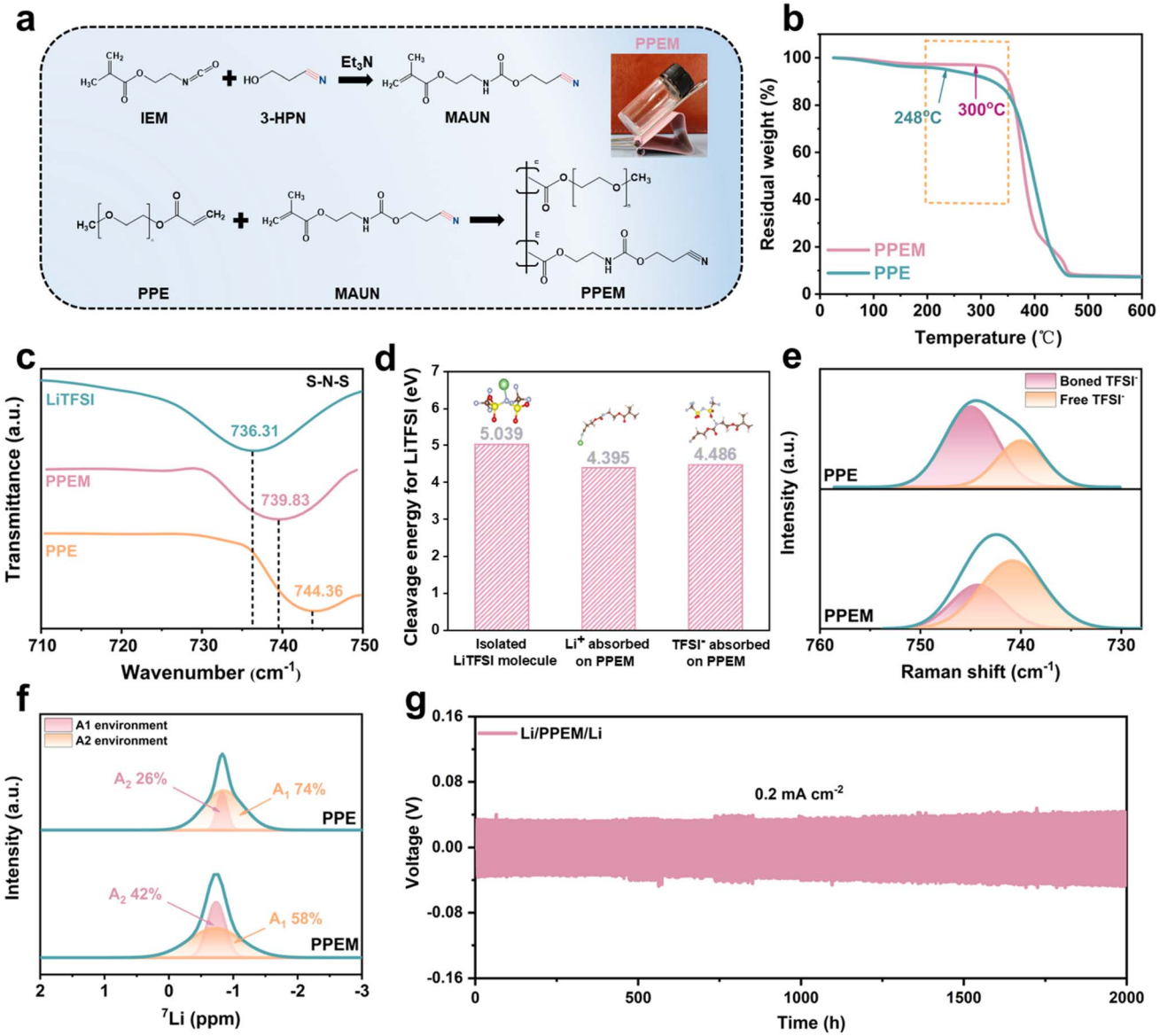

Fig. 1 Characterization of the PPEM polymer. (a) Synthesis schematic diagram of MAUN and PPEM monomer. (b) TGA curves of PPE and PPEM. (c) The infrared amplification spectra of LiTFSI, PPEM, and PPE at the S–N–S bond. (d) Calculation of the dissociation energy of LiTFSI in PPEM. (e) Raman spectra of PPE and PPEM. (f) ^{7}Li solid state NMR spectra of PPE and PPEM electrolytes. (g) Cyclic voltage curves of PPEM on a Li/Li symmetric cell.

current density was increased to 1 mA cm^{-2}, the symmetric cell with PPEM electrolyte demonstrated stable cycling exceeding 900 hours. It exhibited consistent fluctuations in polarization overpotential, which can be attributed to the relatively rapid lithium ion transport at the MAUN/Li interface. Efficient transport ensures uniform deposition of lithium, effectively inhibiting the occurrence of side reactions. Density functional theory (DFT) calculations further elucidated this behavior (Fig. S5), demonstrating that the cyanide group on MAUN (-6.200×10^{-2} eV) exhibits lower electronegativity than the carbonyl oxygen in PEGMA monomers (-4.997×10^{-2} eV), thereby facilitating dissociation and desolvation of Li^{+}. The results of the Raman profiles in Fig. 1e were further confirmed.

Electrochemical characterization and Li^{+} transport mechanism

As depicted in Fig. 2a, the PPEM–LATP composite solid electrolyte, consisting of PPEM and LATP, was prepared using *in situ* polymerization in the initial stage. X-ray diffraction (XRD) analysis revealed no change in crystallinity after incorporating the MAUN matrix; however, the characteristic peaks of the composite solid electrolyte (CSE) exhibited reduced intensity compared to pure LATP (Fig. S6). The chemical interaction between LATP and PPEM was further studied. As shown in Fig. 2b, PPEM–LATP exhibits three new peaks at 3323, 2255, and 1503 cm^{-1}, which can be attributed to the stretching vibrations of –N–H–, –C≡N, and C═O, respectively. A strong interaction

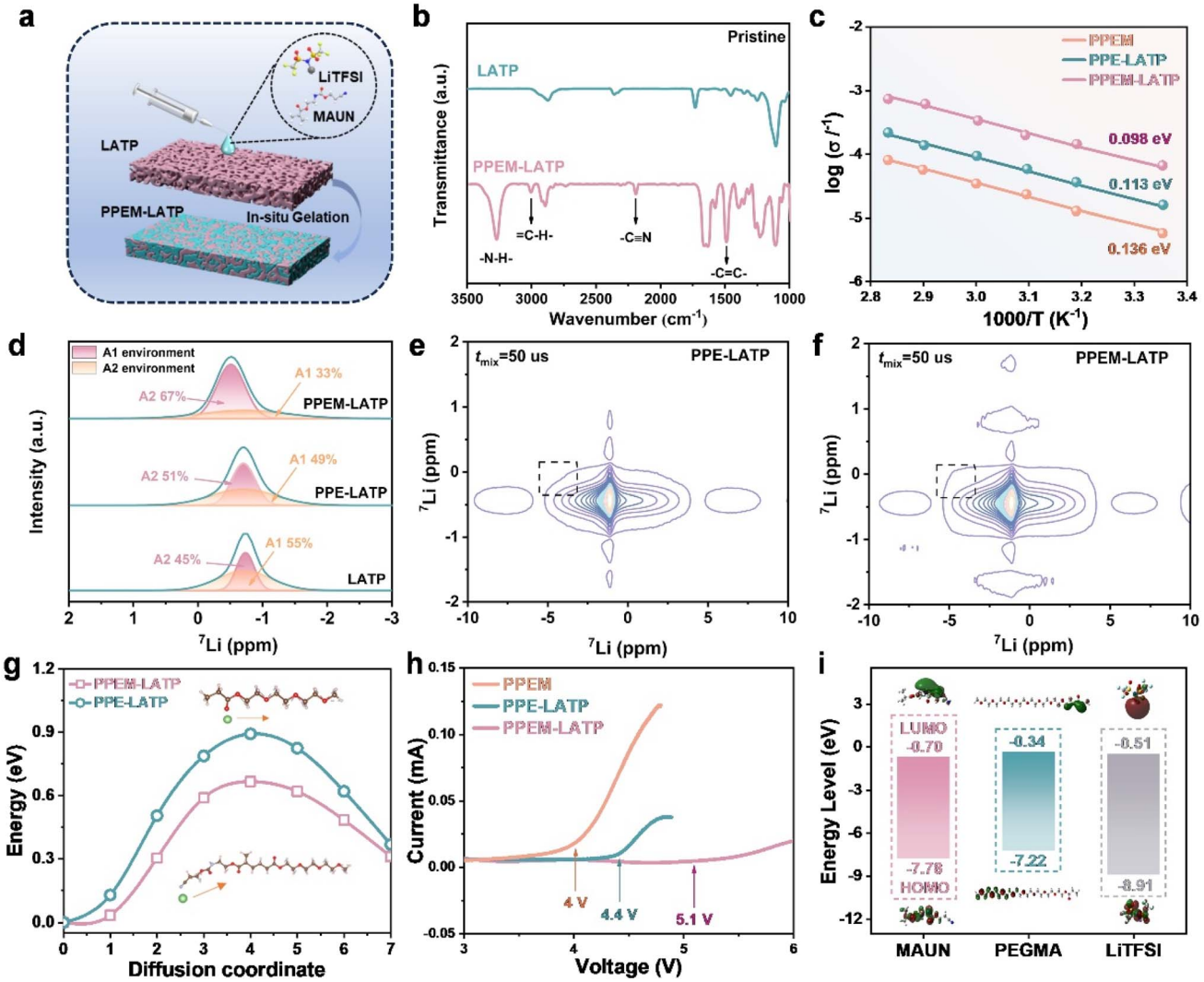

Fig. 2 Electrochemical properties and Li^+ transport mechanism of the PPEM–LATP electrolyte. (a) The schematic diagram for the preparation of PPEM–LATP. (b) FTIR of the LATP and PPEM–LATP. (c) Arrhenius plots of PPEM, PPE–LATP and PPEM–LATP. (d) ^7Li solid state NMR spectra of PPEM–LATP, PPE–LATP, and LATP electrolytes. 2D $^7Li/^7Li$ exchange spectra measured at 298 K for PPE–LATP (e) and PPEM–LATP (f) at $t_{mix} = 50$ ms. (g) Diffusion energy barriers of Li^+ in PPE–LATP and PPEM–LATP. (h) LSV images of PPEM, PPE–LATP and PPEM–LATP. (i) HOMO and LUMO energy levels of MAUN and PEGMA.

between PPEM and LATP was confirmed. The Li^+ transference number (t_{Li^+}) is a critical parameter for evaluating the mobility of Li^+ within electrolytes. As shown in Fig. S7, the t_{Li^+} of the PPEM–LATP composite electrolyte was enhanced to 0.78, as calculated from the polarization current curves and impedance spectra of a Li/PPEM–LATP/Li symmetric cell before and after polarization. The ionic conductivity (σ) was measured at various temperatures, with the room-temperature ionic conductivity increasing from 2.37×10^{-4} S cm^{-1} to 7.2×10^{-4} S cm^{-1} (Fig. S11). Fitting curves (Fig. 2c) indicate that ion transport follows the Vogel–Tammann–Fulcher mechanism. At elevated temperatures, the ionic conductivity of PPEM–LATP reached 10^{-3} S cm^{-1}, suggesting that the incorporation of MAUN shifted Li^+ conduction from a single-mode mechanism relying solely on LATP to a collaborative multi-mode mechanism dominated by LATP and LATP–MAUN interactions.[41] Consequently, the activation energy (E_a) for Li^+ transport in PPEM–LATP was reduced to 0.098 eV (*vs.* 0.180 eV for liquid electrolytes), underscoring its superior ion-conducting capability.[29,30]

^7Li solid-state nuclear magnetic resonance (SS NMR) spectroscopy was performed on the electrolyte to understand the different Li^+ environmental regulation effects of each component. As exhibited in the ^7Li SS NMR in Fig. 2d, the ^7Li resonance at a chemical shift of −0.85 ppm corresponds to the Li^+ interface with LATP. Notably, certain downfield shifts were observed upon introducing the polymer, which resulted in chemical shifts of −0.53 and −0.65 ppm for LATP–PPEM and LATP–PPE, indicating the emergence of an Li^+-conducting highway at the LATP/polymer interface. The proportion of disordered Li^+ environments represented by A_2 increased (67%), confirming that the cyano group of PPEM destroys the strong electrostatic coupling between Li^+ and $TFSI^-$ in LATP,[31–34]

facilitating the rapid migration of Li^+ in the polymer/LATP phase during charging. As shown in Fig. 2e and f, 2D ^7Li–^7Li NMR exchange experiments revealed rapid Li^+ exchange between the PPEM and LATP phases during cycling. The enhanced interface interaction induced by –C≡N promoted the diffusion of Li^+ at the polymer/LATP interface, and the signal intensity increased at 50 ms (*vs.* the initial state in Fig. S12). Density functional theory (DFT) calculations were performed to further understand the underlying mechanisms of rapid kinetics in PPEM–LATP.[35] Furthermore, PPEM–LATP exhibits a lower Li^+ diffusion barrier (0.61 eV) than PPE–LATP (0.88 eV) (Fig. 2g), enabling faster kinetics and uniform Li^+ distribution at the Li anode surface, thereby suppressing dendrite growth and improving cycle life.

Fig. 2h illustrates the electrochemical stability of the electrolytes. Owing to the inherent electrochemical stability of the MAUN and LATP, the electrochemical windows of PPE and PPE–LATP are 4.0 V and 4.5 V, respectively. The electrochemical window of PPEM–LATP is further enhanced to 5.4 V. The robust interfacial layer was enriched with Li_3N, Li_xNO_y species, and O–C=O functionalities at the electrode–electrolyte interface. Such a layer not only suppresses deleterious side reactions between PEGMA and the lithium anode but also dynamically transforms into a Li^+-permeable conduit under high-voltage stress, circumventing oxidative degradation of PEGMA.[36–38] Further insights were obtained from the DFT simulations of the frontier molecular orbitals of the electrolyte (Fig. 2i). The LUMO energy level of MAUN (−0.70 eV) is lower than that of LiTFSI (−0.51 eV), endowing MAUN with superior electron-accepting capability at the lithium–metal interface and yielding a thermodynamically stable SEI layer. Beyond passivating interfacial reactivity, this redox-active layer assumes a dual role: it preserves Li^+ transport pathways even under harsh oxidative potentials, effectively decoupling ion conduction from cathodic decomposition pathways.

Dynamic interfacial and structural analysis

Galvanostatic cycling tests were conducted on Li‖Li batteries assembled with PPEM–LATP and PPE–LATP electrolytes at a current density of 0.2 mA cm^{-2} and 30 °C to assess interfacial stability with lithium metal anodes. As shown in Fig. 3a, the lithium symmetrical battery assembled with the PPE–LATP electrolyte showed a significant increase in overpotential after 800 h of cycling, which was attributable to the nonuniform electric field distribution at the Li/LATP interface. Owing to the uneven distribution of the electric field at the Li/LATP interface and the uneven growth of the interface phase, stress concentration occurred in the edge region of the interface in contact with LATP. Progressive stress accumulation leads to electrolyte fracture, elevated interfacial resistance, and eventual battery failure. In contrast, the PPEM–LATP-based cell demonstrated excellent cycle stability, maintaining stable operation for over 2400 h at 0.2 mA cm^{-2} with minimal polarization voltage. The enhanced compatibility between PPEM–LATP and lithium metal is likely due to PPEM's dual role as an ion-conductive interlayer that reduces interfacial resistance while suppressing LATP reduction. To further validate the stabilizing effect of MAUN on the electrode/electrolyte interface, XPS analysis was performed on the Ti 2p spectra of the PPEM–LATP electrolyte after cycling (Fig. 3b). Only two peaks at 465.6 eV and 459.8 eV were observed, corresponding exclusively to the Ti^{4+} oxidation state, confirming intact Ti chemistry. In contrast, PPE–LATP

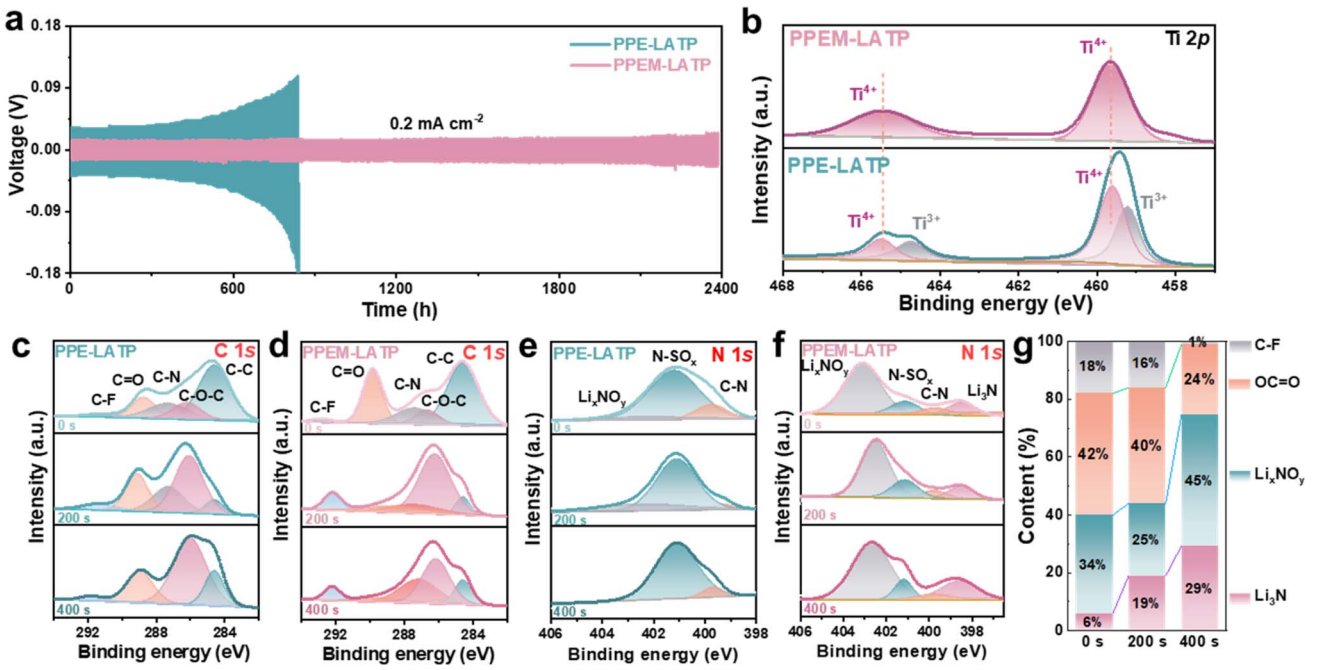

Fig. 3 Anode stability analysis of the PPEM–LATP electrolyte. (a) Li//Li symmetrical battery with PPEM–LATP at a current density of 0.2 mA cm^{-2}. (b) XPS spectra of Ti 2p in Li//Li cells with PPE–LATP and PPEM–LATP after cycles. (c–f) XPS spectra of C 1s and N 1s in Li//Li cells with PPE–LATP and PPEM–LATP after 10 cycles. (g) Relative contents of C–F, O–C=O and Li_3N in SEI layers at different etching depths.

electrolytes showed additional peaks at lower binding energies, indicative of reduced Ti species (*e.g.*, Ti^{3+} or Ti^{2+}),[39] indicating the unsaturated cyanide groups in PPEM coordinate strongly with Ti^{4+} within LATP pores, blocking direct contact between Li metal and LATP. Such coordination effectively inhibits LATP reduction and associated parasitic reactions, thereby stabilizing the electrode–electrolyte interface.

To elucidate the enhanced compatibility between PPEM–LATP and lithium metal, XPS sputtering analysis was performed on cycled lithium metal surfaces to characterize the chemical composition of the solid electrolyte interphase (SEI). As depicted in Fig. 3d, the C 1s spectrum of PPEM–LATP-derived SEI layers exhibited three dominant peaks: C–C (≈284.8 eV), O–C=O (≈286.6 eV), and C–F (≈292.4 eV). Notably, the intensities of the C–F and O–C=O peaks diminished with increasing sputtering time, indicating their prevalence in the surface region.[40–42] In the N 1s spectrum (Fig. 3f), prolonged sputtering revealed the progressive enrichment of Li_3N (≈398.5 eV) at the inner layers of the SEI, confirming the formation of a graded SEI architecture. This hierarchical structure comprises a surface organic layer rich in C–F and O–C=O moieties and an inorganic Li_3N-rich core. The polar C–F bonds act as effective Lewis base sites for Li^+ adsorption, while the inorganic Li_3N reinforces mechanical stability and facilitates rapid Li^+ transport. Moreover, the high ionic conductivity, low diffusion barrier, and thermal stability of Li_3N suppress interfacial side reactions and enable sustained performance at elevated temperatures.

The prepared precursor solution was evenly dropped onto both sides of the porous LATP ceramic sheet, and the assembled battery was left to stand for a period to allow the precursor solution to fully impregnate the ceramic sheet (Fig. S13). The polymerization process was completed by maintaining the battery at 60 °C for 8 h. Fig. 4a and b illustrate the highly ordered LATP porous structure that optimizes the lithium-ion transport pathway. Cross-linking polymerization with PPEM not only improves ionic conductivity, but also enhances mechanical stability, making the composite electrolyte more durable under extreme conditions, such as high temperatures. Scanning

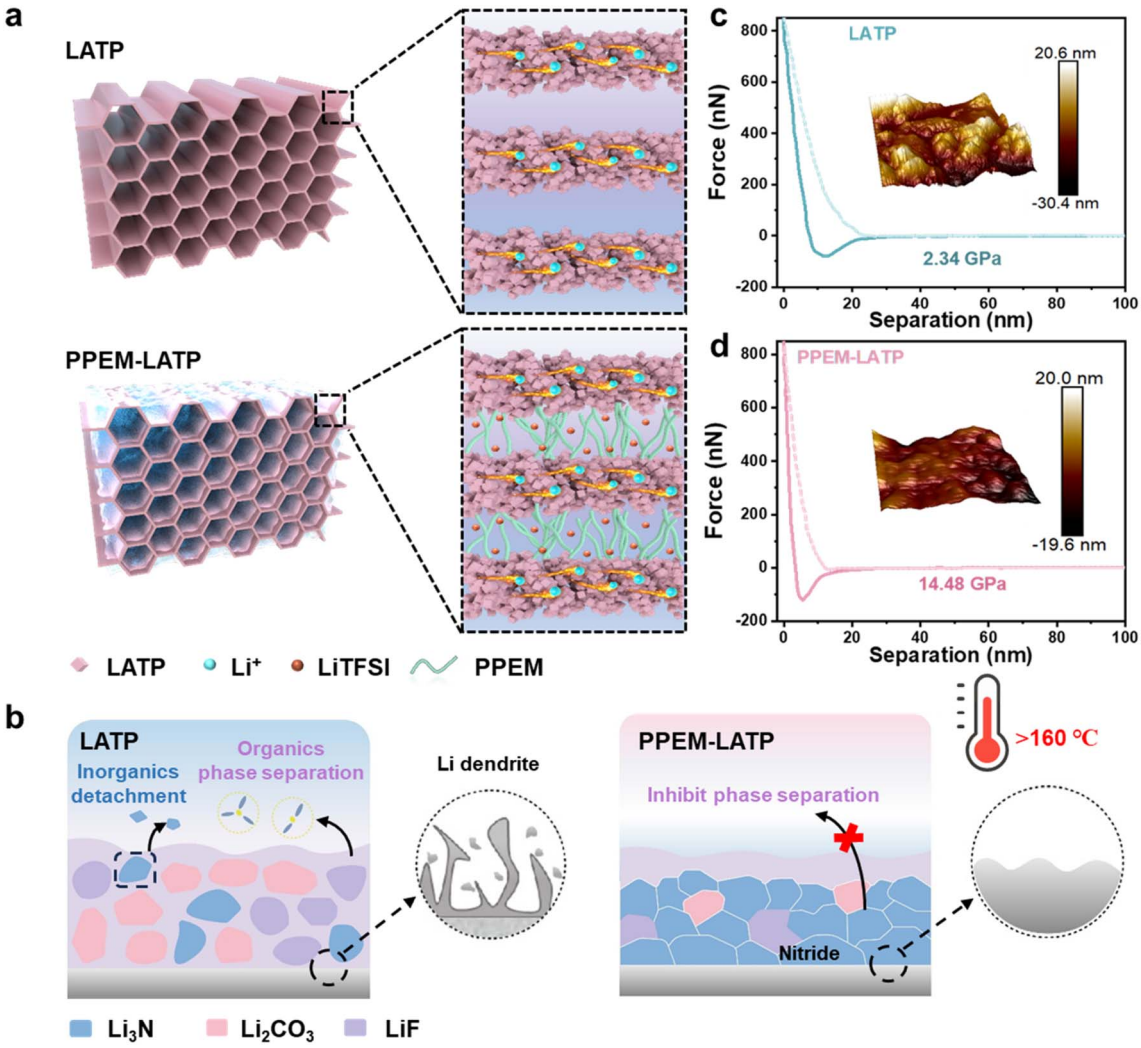

Fig. 4 Characteristics of composite solid-state electrolytes for all-around-safety lithium batteries. (a) Schematic illustration of *in situ* polymerization to prepare the PPEM–LATP composite solid electrolyte. (b) Diagram of the SEI after cycling of LATP and PPEM–LATP in a 160 °C environment. AFM testing of post-cycling: (c) LATP and (d) PPEM–LATP lithium anode surface roughness and force–displacement curves.

electron microscopy (SEM) images (Fig. S9) revealed the interconnected porous structure of LATP ceramic scaffolds, while uniform elemental distribution in EDS mapping confirmed homogeneous PPEM infiltration into the LATP matrix (Fig. S10), effectively sealing micro-pores within the composite architecture. AFM characterization (Fig. 4c and d) further corroborated these findings: PPEM–LATP yielded a smoother SEI surface (lower roughness) and higher Young's modulus ($\approx$14.48 GPa *vs.* 2.34 GPa for PPE–LATP). The crosslinked PPEM network forms a robust organic shell atop the inorganic Li_3N layer, enhancing resilience to lithium volume expansion and stabilizing long-term cycling. SEM analysis (Fig. S14a and b) revealed stark differences in SEI morphology: Li/PPEM–LATP/Li cells maintained a 35 μm-thick compact SEI layer after 2400 h of cycling, whereas Li/PPE–LATP/Li cells exhibited a 66 μm-thick porous SEI after only 800 h, leading to catastrophic impedance rise and failure. The denser PPEM-derived SEI promoted uniform lithium deposition and mitigated dendrite growth.

High temperature performance

The long-term cyclability of the composite electrolyte was assessed using Li//$LiFePO_4$ (LFP) pouch cells. As shown in Fig. S15, the Li/PPEM–LATP/LFP cell delivered an initial discharge capacity of 137.7 mAh g^{-1} at 0.2C and retained 90.14% capacity after 200 cycles (CE: 99.79%), outperforming the Li/PPE–LATP/LFP cell (initial capacity: 126.3 mAh g^{-1},

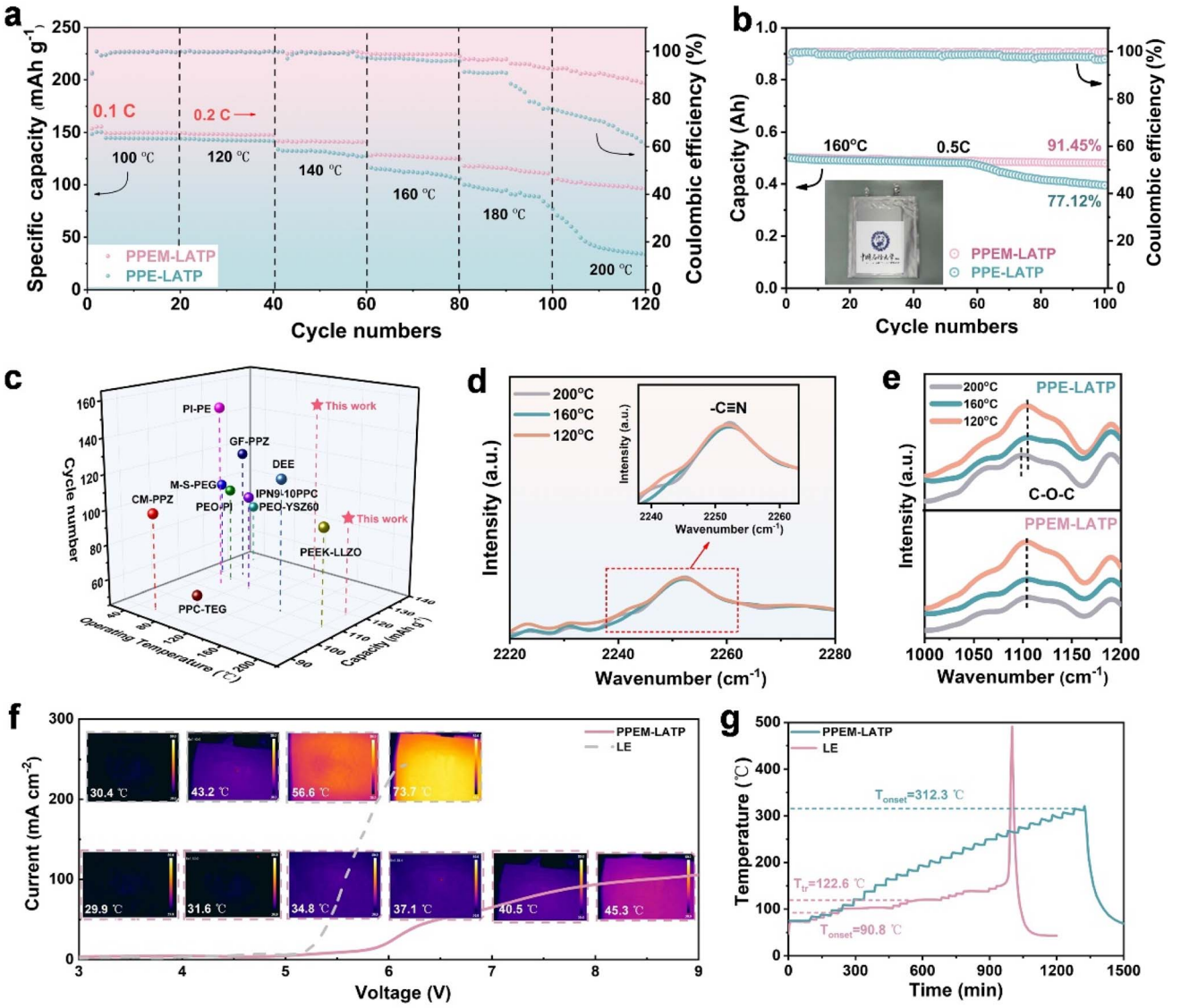

Fig. 5 Li battery performance under abuse conditions. (a) High temperature performance of cells with PPE–LATP and PPEM–LATP from 100 °C to 200 °C. (b) Cycle performance at 160 °C and 0.5C rate for graphite/PPE–LATP/LFP and graphite/PPEM–LATP/LFP pouch cells. ≡ (c) Comparison of cycle performance of PPEM–LATP with other CSEs in a high-temperature environment. FT-IR spectra of –C≡N (d) And –C–O–C– (e) after cycling at different temperatures. (f) LSV curves and the corresponding infrared thermal imaging photographs of Li/PPE–LATP/LFP and Li/PPEM–LATP/LFP pouch cells at a scan rate of 20 mV s^{-1} from the open circuit voltage to 9 V. (g) Temperature changes of fully charged 0.5 Ah LFP/graphite pouch cells with BASE electrolyte and PPEM–LATP electrolyte in ARC tests.

65.22% retention after 200 cycles). Elevated-temperature testing (Fig. 5a) further validated the robustness of PPEM–LATP: at 100 °C, the cell maintained a capacity of 131.8 mAh g^{-1} over 40 cycles (CE: 99.72%). When the temperature was incrementally increased to 200 °C, the capacity retention stabilized at ~81.7% after 120 cycles, whereas that of the PPE–LATP counterpart dropped to 38.2%. These results underscore the exceptional thermal tolerance of PPEM–LATP, enabling stable operation even at 160 °C. Post-mortem XPS analysis of the cycled Li anode (Fig. S16a and b) revealed a graded SEI layer comprising inner Li_3N and outer organic components, which synergistically suppresses volumetric changes during cycling while maintaining facile Li^+ transport. To simulate practical applications (Fig. 5b), Li metal micro-pouch cells (graphite/PPEM–LATP/LFP) were fabricated and tested at 160 °C/0.5C. The PPEM–LATP cell delivered an initial capacity of 0.51 Ah with 91.45% retention after 100 cycles, surpassing the PPE–LATP cell (0.49 Ah, 77.12% retention) by a significant margin. Compared to the recently reported CSE, PPEM–LATP provides lithium–metal batteries with unprecedented advantages in terms of capacity, operating temperature, and lifetime (Fig. 5c and SI Table S1).

The structural and chemical evolution of the electrolytes under thermal abuse conditions was investigated *via ex situ* attenuated total reflection infrared (ATR) spectroscopy and X-ray diffraction (XRD). As shown in Fig. 5d and e, the free C–O–C stretching band in PPE–LATP exhibited a continuous redshift from 1103.52 cm^{-1} to 1099.69 cm^{-1} with increasing temperature, indicating ether bond cleavage induced by oxidative decomposition. In stark contrast, the –C≡N stretching mode in PPEM–LATP remained nearly invariant at 2255 cm^{-1}, and the C–O–C peak retained its initial position (1103.52 cm^{-1}).[43] The strong ligand coordination between cyanide groups and transition metals on the electrode surface shields reactive species and inhibits cathodic driven ether oxygen bond decomposition. XRD analysis (Fig. S17) confirmed that PPEM–LATP retained its crystalline LATP structure (#35-0754) even after 100 cycles at 160 °C, demonstrating the formation of a graded SEI layer enhanced by the outer organic layer. By acting as a physical barrier for anode derived reaction species, it promoted uniform lithium coating, inhibited dendrite growth, and maintained LATP integrity. LFP/graphite pouch cell was subjected to overcharge abuse (0.5C, 20 mV s^{-1}) to evaluate safety performance (Fig. 5f). The $LiPF_6$-EC:DMC-based cell exhibited a sharp increase in current density at 5.2 V, with surface temperature soaring to 73.7 °C at 6.1 V—a hallmark of SEI decomposition-triggered thermal runaway. In contrast, the PPEM–LATP cell maintained stable current density up to 9 V, with surface temperature capped below 50 °C. The superior oxidative stability of PPEM–LATP, coupled with its crosslinked polymer network, enables the formation of a robust gradient SEI layer that suppresses cathode-side parasitic reactions. As shown in Fig. 5g, accelerating rate calorimetry (ARC) tests further validated the thermal safety advantages of PPEM–LATP. The 0.5 Ah 100% SOC LFP/graphite pouch cells using $LiPF_6$/EC–DMC electrolyte underwent severe thermal runaway at T_{tr} = 122.6 °C, culminating in a catastrophic T_{max} = 496 °C. Strikingly, for 0.5 Ah 100% SOC LFP/graphite pouch cells using PPEM–LATP, no severe thermal runaway occurred below 312.3 °C. This 60% suppression in thermal runaway severity highlights PPEM–LATP's ability to mitigate thermal propagation in LFP/graphite full cells.

Conclusions

A cyanate-functionalized polymer/ceramic composite electrolyte (PPEM–LATP) was engineered to address critical challenges in high-temperature lithium–metal batteries. The dual-functional design integrates interfacial stabilization and dynamic SEI healing mechanisms to improve interfacial compatibility and thermal stability at high temperatures. Cyano groups in PPEM form strong coordination bonds with Ti^{4+} sites on LATP, preventing ceramic/polymer phase separation at elevated temperatures. PPEM enables the *in situ* formation of a gradient SEI layer, featuring an inner Li_3N-rich layer for high ionic conductivity and an outer crosslinked polymer layer (C–F and O–C═O bonds) for mechanical robustness. This architecture heals microcracks during cycling and maintains a stable Li^+ flux. The assembled Li//Li symmetric cells exhibited stable polarization performance over 2400 h of cycling, with no significant signs of uneven lithium deposition on the anode surface after cycling. The graphite/PPEM–LATP/LFP mini-pouch cell (0.5 Ah) assembled with this composite electrolyte maintained a capacity retention of over 91% after 100 cycles at a C-rate of 0.5C and 160 °C, with a stable coulombic efficiency above 99%. A novel design concept has been introduced for composite solid electrolytes, ensuring high safety and compatibility, and highlighting the critical role of high Li^+ transference numbers, ionic conductivity, and stable SEI layers in achieving stable operation under extreme conditions.

Author contributions

Jakai Wang: investigation, data curation, conceptualization, formal analysis, validation, writing–original draft. Siyu Zhang: conceptualization, writing–review & editing, supervision, funding acquisition. Linchen Zhang, Shenzhen Deng: formal analysis, data curation, conceptualization, validation. Yuanyuan Sun: data curation, conceptualization, validation. Yimou Wang, Jinglin Wang: supervision, validation, conceptualization. Junfeng Qin: supervision, validation. Weidong Zhou, Mingbo Wu: supervision, validation, funding acquisition. Zhongtao Li: writing–review & editing, funding acquisition, supervision.

Conflicts of interest

There are no conflicts to declare.

Data availability

The data that support the findings of this study are available within the article and its SI or from the corresponding author upon reasonable request. The supplementary information comprehensively details: (1) experimental procedures including the synthesis of cyanate-functionalized MAUN monomer, fabrication of hierarchical 3D LATP frameworks *via* PMMA-

templated calcination, preparation of PPEM polymer precursor solutions with LiTFSI/AIBN, and assembly protocols for coin/pouch cells; (2) electrochemical testing methodologies (EIS, charge–discharge cycling, thermal runaway analysis *via* ARC) and materials characterization (NMR, FTIR, XRD, XPS, SEM/EDX); (3) computational details for DFT calculations; (4) SI Fig. S1–17 (spectroscopic/morphological analyses, electrochemical performance, thermal stability data) and Table S1 benchmarking high-temperature cycling performance against state-of-the-art solid electrolytes. The data ensure full reproducibility and transparency. See DOI: **https://doi.org/10.1039/d5sc05102a**.

Acknowledgements

We thank the support of the National Natural Science Foundation of China (22261160570, 22409215), project 2025HWYQ-037 supported by Shandong Provincial Natural Science Fund for Excellent Young Scientists Fund Program (Overseas), Taishan Scholar Project (tsqn202312113), and China University of Petroleum (East China) Independent Innovation Research Program Project (25CX06008A).

References

1 X. B. Han, S. Y. Ma, Y. Wang, Y. Lu and O. Minggao, *Nat. Commun.*, 2025, **16**, 3699.
2 X. Su, X. P. Xu, Z. Q. Ji and J. Wu, *Electrochem. Energy Rev.*, 2024, **7**, 2.
3 Z. Zhang and W.-Q. Han, *Nano-Micro Lett.*, 2024, **16**, 24.
4 B. Zhao, W. C. Ma, B. B. Li and X. T. Hu, *Nano Energy*, 2022, **91**, 106643.
5 X. E. Wang, R. Kerr, F. F. Chen, N. Goujon and J. M. Pringle, *Adv. Mater.*, 2020, **32**, 1905219.
6 H. L. Wan, J. J. Xu and C. S. Wang, *Nat. Rev. Chem.*, 2023, **8**, 30–44.
7 W. Liu, N. Liu, J. Sun, P. C. Hsu, Y. Z. Li, H. W. Lee and Y. Cui, *Nano Lett.*, 2015, **15**, 2740–2745.
8 Z. S. Zhao, X. Y. Zhou, B. Zhang, F. F. Huang, Y. Wang, Z. S. Ma and J. Liu, *Angew. Chem., Int. Ed.*, 2023, **62**, e202308738.
9 Y. Guo, S. C. Wu, Y. B. He, F. Y. Kang, L. Q. Chen and Q. H. Yang, *eScience*, 2022, **2**, 138–163.
10 P. C. Li, C. Y. Ma, D. B. Kong and Z. T. Li, *Adv. Mater.*, 2025, **37**, 2418990.
11 Q. K. Zhang, X. Q. Zhang, J. Wan, N. Yao, T. L. Song, J. Xie and J. Q. Huang, *Nat. Energy*, 2023, **8**, 725–735.
12 P. Ding, Z. Lin, X. Guo, L. Wu, Y. Wang, H. Guo and H. Yu, *Mater. Today*, 2021, **51**, 449–474.
13 X. X. Liu, L. Pan, H. T. Zhang, C. C. Liu, M. F. Cao, M. Gao, Y. Zhang, Z. Y. Xu, Y. P. Wang and Z. M. Sun, *Nano-Micro Lett.*, 2025, **17**, 249.
14 L. Z. Fan, H. C. He and C. W. Nan, *Nat. Rev. Mater.*, 2021, **6**, 1003–1019.
15 Y. P. Wang, P. C. Yuan, X. X. Liu, S. F. Feng, M. F. Cao, J. X. Ding, J. C. Liu, T. Hihara, L. Pan and Z. M. Sun, *Adv. Funct. Mater.*, 2024, **34**, 2405060.
16 J. Yang, R. R. Li, P. P. Zhang, J. M. Zhang, J. Meng, Z. Li and X. Pu, *Energy Storage Mater.*, 2024, **64**, 103088.
17 X. X. Liu, L. Pan, H. T. Zhang, P. C. Yuan, M. F. Cao, Y. P. Wang, Z. Y. Xu, M. Gao and Z. M. Sun, *Nano-Micro Lett.*, 2025, **17**, 190.
18 Y. Jin, K. Liu, J. L. Lang, D. Zhuo, Z. Y. Huang, C. A. Wang and Y. Cui, *Nat. Energy*, 2018, **3**, 732–738.
19 Y. R. Xiao, K. Turcheniuk, A. Narla, A. Y. Song, X. L. Ren, A. Magasinski and G. Yushin, *Nat. Mater.*, 2021, **20**, 984–990.
20 D. H. Tan, A. Banerjee, Z. Chen and Y. S. Meng, *Nat. Nanotechnol.*, 2020, **15**, 170–180.
21 J. L. Chen, Y. Lin, Q. Li, H. Ren, L. C. Zhang, W. D. Zhou and Z. T. Li, *Angew. Chem., Int. Ed.*, 2024, **63**, e202407024.
22 L. Z. Fan, H. C. He and C. W. Nan, *Nat. Rev. Mater.*, 2021, **6**, 1003–1019.
23 L. Wang, S. G. Xu, Z. Wang, E. E. Yang, W. Y. Jiang, S. H. Zhang, X. G. Jian and F. Y. Hu, *eScience*, 2023, **3**, 100090.
24 H. R. Zhang, L. Huang, H. T. Xu, X. H. Zhang, Z. Chen, C. H. Gao, C. L. Lu and G. L. Cui, *eScience*, 2022, **2**, 201–208.
25 D. Lin, Y. Liu and Y. Cui, *Nat. Nanotechnol.*, 2017, **12**, 194–206.
26 C. W. Wang, W. W. Ping, Q. Bai, H. C. Cui, R. Hensleigh, R. L. Wang, A. H. Brozena, Z. P. Xu, J. Q. Dai, Y. Pei and L. B. Hu, *Science*, 2020, **368**, 521–526.
27 X. G. Han, Y. H. Gong, K. Fu, X. F. Hu, G. T. Hitz, J. Q. Dai, A. Pearse, B. Y. Liu, H. Wang, G. Rublo and L. B. Hu, *Nat. Mater.*, 2017, **16**, 572–579.
28 Y. R. Xiao, K. Turcheniuk, A. Narla, A. Y. Song, X. K. Ren, A. Magasinski, A. Jain, S. Huang, H. Lee and G. Yushin, *Nat. Mater.*, 2021, **20**, 984–990.
29 R. Lv, W. Kou, S. Guo, W. Wu and Y. Zhang, *Angew. Chem., Int. Ed.*, 2022, **61**, e202114220.
30 Y. M. Jin, R. F. Lin, Y. M. Li, X. B. Zhang, S. P. Tan, Y. Shuai and Y. P. Xiong, *Angew. Chem., Int. Ed.*, 2024, **63**, e202403661.
31 W. J. Ji, B. Luo, Q. Wang, G. H. Yu, Z. X. Zhang, Y. Tian, Z. W. Zhao, R. R. Zhao, S. B. Wang, X. W. Wang, B. Zhang, J. F. Zhang and J. Liang, *Nat. Commun.*, 2024, **15**, 9920.
32 S. Huang, Z. Wu, B. Johannessen, K. Long, P. Qing, P. He, Y. Chen and L. Chen, *Nat. Commun.*, 2023, **14**, 5678–5689.
33 P. Xu, Y. C. Gao, Y. X. Huang, Z. Y. Shuang, W. J. Kong, X. Y. Huang, W. Z. Huang, N. Yan and Q. Zhang, *Adv. Mater.*, 2024, **36**, 2409489.
34 Q. Lv, Y. Y. Sun, S. S. Jiang, H. Ren, Y. Lin, Q. Li, L. P. Lu, M. B. Wu and Z. T. Li, *J. Mater. Chem. A*, 2024, **12**, 28224.
35 Y. B. He, C. Y. Wang, R. Zhang, P. C. Zou, Z. Y. Chen, S. M. Bak, S. E. Trask, Y. H. Du and H. L. Xin, *Nat. Commun.*, 2024, **15**, 10015.
36 X. Ren, L. Zou, S. Jiao, D. Mei, M. H. Engelhard, Q. Li, B. D. Adams and C. Wang, *ACS Energy Lett.*, 2019, **4**, 896–902.
37 Y. B. Mu, L. Yang, Y. T. Feng, H. C. Gu, Z. Y. Zou, Y. Q. Chu, Z. Y. Zhou, T. S. Zhao and L. Zeng, *Nano Energy*, 2025, **138**, 110885.
38 L. M. Suo, W. J. Xue, M. Gobet, S. G. Greenbaum, C. Wang, Y. M. Chen, W. L. Yang and J. Li, *Proc. Natl. Acad. Sci. U. S. A.*, 2018, **115**, 1156–1161.
39 M. Yao, J. Y. Liang, T. T. Zuo, Y. X. Yin, S. Xin, S. J. Tan and Y. G. Guo, *Adv. Funct. Mater.*, 2020, **30**, 1908047.

40 W. J. Ren, X. C. Shang, Y. Lin, H. Ren, L. C. Zhang, M. B. Wu and Z. T. Li, *Adv. Energy Mater.*, 2025, **15**, 2405284.
41 C. Wang, T. Wang, L. L. Wang, Z. L. Hu, Z. L. Cui, J. D. Li, S. M. Dong, X. H. Zhou and G. L. Cui, *Adv. Sci.*, 2019, **6**, 1901036.
42 D. M. Dai, P. Y. Yan, G. H. Liu, Z. Z. Zhang, J. Z. Guo, B. Li and X. L. Wu, *Adv. Funct. Mater.*, 2025, 2503696.
43 Z. L. Lv, Q. Zhou, S. Zhang, S. M. Dong, Q. L. Wang, L. Huang, K. Chen and G. L. Cui, *Energy Storage Mater.*, 2021, **37**, 215–223.